

Active Site and Electronic Structure Elucidation of Pt Nano- particles Supported on Phase-pure Molybdenum Carbide Nanotubes

Lucun Wang, Shibely Saha, Rebecca
Fushimi, Dongmei Li, Shuai Tan

March 2017



The INL is a U.S. Department of Energy National Laboratory
operated by Battelle Energy Alliance

Active Site and Electronic Structure Elucidation of Pt Nano-particles Supported on Phase-pure Molybdenum Carbide Nanotubes

Lucun Wang, Shibely Saha, Rebecca Fushimi, Dongmei Li, Shuai Tan

March 2017

**Idaho National Laboratory
Idaho Falls, Idaho 83415**

<http://www.inl.gov>

**Prepared for the
U.S. Department of Energy
Office of Nuclear Energy
Under DOE Idaho Operations Office
Contract DE-AC07-05ID14517**

Active Site and Electronic Structure Elucidation of Pt Nanoparticles Supported on Phase-pure Molybdenum Carbide Nanotubes

Shuai Tan ^{a,c}, Lucun Wang ^{b,c}, Shibely Saha ^a, Rebecca R Fushimi ^{b,c}, Dongmei Li ^{a,c,*}

^a Department of Chemical Engineering, University of Wyoming, Laramie, WY 82071, USA

^b Biological and Chemical Processing Department, Energy and Environment Science and Technology, Idaho National Laboratory, Idaho Falls, ID, USA 83415

^c Center for Advanced Energy Studies, Idaho Falls, ID, USA 83401.

Supporting Information Placeholder

ABSTRACT: We recently showed that phase-pure molybdenum carbide nanotubes can be durable supports for Pt nanoparticles in hydrogen evolution reaction (HER). Here we characterize surface properties of the same Pt/ β -Mo₂C catalyst platform using carbon monoxide (CO)-Pt and CO-Mo₂C bond strength of different Pt particle sizes in the < 3 nm range. Results from diffuse reflectance infrared Fourier transform spectroscopy (DRIFTS) and temporal analysis of products (TAP) revealed the existence of different active sites as Pt particle size increases. Correlation between the resultant catalyst activity and deposited Pt particle size was further investigated using water-gas-shift (WGS) as a probe reaction, suggesting that precise control of particle diameter and thickness is needed for optimized catalytic activity.

Early work of Levy and Boudart¹ indicated the platinum (Pt)-like properties of transition metal carbides (TMCs), resulting from their similarity to Pt in geometric and electronic structures. Recent work has focused on replacing Pt with TMCs in electrochemical devices, such as PEMFC and electrolyzers.²⁻⁵ Catalytic properties of TMCs, especially molybdenum carbide (Mo₂C) and Pt/Mo₂C, for low temperature water gas shift (WGS) have also been investigated.⁶⁻¹¹ Schweitzer *et al.* reported the superiority of Pt/Mo₂C catalyst over the oxide supported catalysts and predicted that the WGS reaction occurred near the Pt/Mo₂C interface, followed by computational simulation.¹¹ Using both *ex situ* and *in situ* x-ray absorption (XAS), Sabins *et al.* found that the synergy between Pt-Mo alloy nanoparticle and Mo₂C was the cause for the enhanced Pt/Mo₂C activity.^{8,9} Despite the comprehensive investigation on the origin of the enhanced catalytic activity of Pt/Mo₂C catalysts relative to bare Mo₂C, there still lacks study on how the size of supported noble metal, such as Pt, affects resultant metal/carbide catalyst activity when: 1) both the TMC support and deposited metal particles are in the nano-scale regime; 2) the carbide support has pristine phase purity.

Chemical properties of supported metals can be attributed to two effects: ligand and strain effect.^{12,13} Ligand effect results from orbital interaction between a deposited metal and its

support, inducing electronic charge transfer at the interface, while strain effect results from lattice mismatch. These effects often result in d-band center shift and, consequently, changes in metal-adsorbate bond strength and catalytic reactivity of resultant catalysts.¹⁴⁻¹⁶ Here we report a unique Pt/Mo₂C catalyst platform where phase-pure Mo₂C nanotube was used as a support, with Pt deposited onto the support in a rotary atomic layer deposition (ALD) reactor.² Such atomic level size control has only been achieved on oxide supports¹⁷⁻¹⁹ until recently.²⁰ In contrast to the mesoporous Mo₂C structures used in open literature,⁸ which makes imaging studies difficult, the phase-pure Mo₂C nanotube in our recent study provides much-needed detail of Pt lattice as Pt particle size grows from atomic to 2-3 nm.²⁰ Specifically, 15, 50 and 100 ALD cycles were chosen based on pioneering work,²¹ with resultant samples referred to as 15, 50 and 100 Pt/Mo₂C.

Table.S1 summarizes Pt mass loading, Brunauer, Emmett and Teller (BET) surface area and Pt NP sizes. We note that mass loading of Pt in 15 Pt/Mo₂C sample was too small to be detected using inductively coupled optical emission spectrometry (ICP-OES). Pt particle size measured by hydrogen (H₂) chemisorption increased from 0.2-0.3 nm in 15 Pt/Mo₂C to ~2 nm in 50 Pt/Mo₂C sample and to ~2.7 nm Pt particles size in 100 Pt/Mo₂C, consistent with size measurement using transmission electron microscopy (TEM) images (Fig.S2). It should be noted that no H₂ adsorption was observed from bare Mo₂C samples, confirming that Pt are the only H₂ absorption sites. Different from the raft-like Pt particles supported on Mo₂C reported by Schweitzer *et al.*,¹¹ both TEM images and Pt dispersion suggest that NPs of 50 Pt/Mo₂C have smaller diameter (2 nm) and are thinner than those in 100 Pt/Mo₂C (2.7 nm). In other words, as the Pt particles grow in diameter with increasing ALD cycles, their thickness also increases. While TEM images qualitatively revealed this trend, the higher dispersion in 50 Pt/Mo₂C (57%) than 100 Pt/Mo₂C (41%) measured via H₂ chemisorption quantitatively proved this observation. As shown in Fig. S3, 50 Pt/Mo₂C samples also have the largest binding energy (BE) shift (0.70 eV) from Pt⁰ (74.5 eV in 4f_{5/2}) among the 15, 50 and 100 Pt/Mo₂C samples, indicating strongest interaction between Pt NPs and the Mo₂C nanotube

support.²⁰ Mun et al.²² attributed the core-level shift to electron transfer between Pt atom and its support, often referred to as ligand effect.¹² We recently demonstrated that strain effect from the metal-support lattice mismatch is also responsible for enhanced electrochemical activity of resultant catalysts (Fig.S4 and S5).²⁰ We hypothesize that smaller and thinner Pt particles of 50 Pt/Mo₂C possess more substantial amount of sites affected by the strain-ligand effect than those in 100 Pt/Mo₂C NPs. Thicker particles allow Pt sites on top surface to be excluded from the strain-ligand effect.

To experimentally correlate the strain-ligand effect with Pt-adsorbate bond strength for different Pt NP sizes, diffuse reflectance infrared Fourier transform spectroscopy (DRIFTS) was utilized to characterize CO adsorption on Pt/Mo₂C.^{19,23,24} Temperature programmed desorption (TPD) was carried out for both bare Mo₂C and Pt/Mo₂C samples. Since all samples are black powders, they were diluted to 1% (wt) in potassium bromide (non-absorbing matrix) to ensure strong scattered light signals. Fig. S6 provides the peaks for CO molecules adsorbed on Mo₂C sites (CO-Mo₂C) as a baseline. For 50 and 100 Pt/Mo₂C samples, two additional peaks were observed. A unique peak at 2165 cm⁻¹ was observed with 50 Pt/Mo₂C, which was assigned to CO molecules adsorbed on cationic Pt atoms (CO-Pt^{δ+}).¹⁹ A wide peak at low intensity (2030-2070 cm⁻¹) for 50 Pt/Mo₂C was assigned to CO molecules linearly adsorbed on Pt⁰ sites (CO-Pt⁰), while two separate peaks (2064 and 2087 cm⁻¹) were present for CO-Pt⁰ bonds on 100 Pt/Mo₂C surface. The less significant peak at 2087 cm⁻¹ that appeared after 5 min of He purging at 150°C was speculated to be the CO molecules linearly adsorbed onto weakly coordinated Pt⁰ at larger Pt particles >3 nm.²⁵

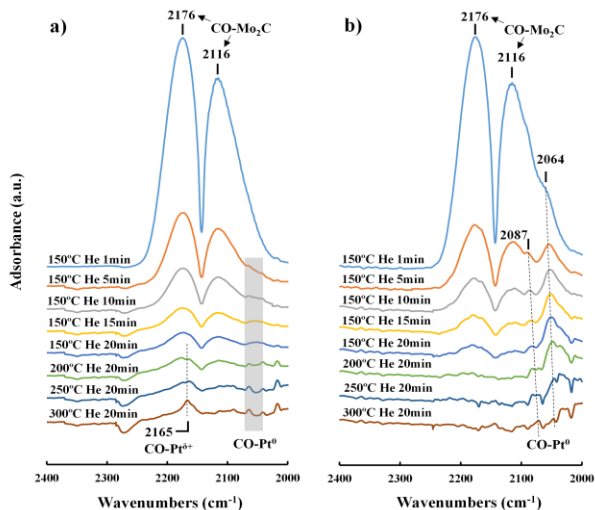


Figure 1. DRIFTS results of CO-TPD under different helium purging time and temperatures on: a) 50 Pt/Mo₂C and b) 100 Pt/Mo₂C.

We note that there is a lack of CO-Pt^{δ+} signals from 100 Pt/Mo₂C, compared to 50 Pt/Mo₂C, indicating that thicker Pt particles have substantially less Pt atoms impacted by strain-ligand effect since Pt^{δ+} sites are the results of strong ligand-strain effect. In other words, the higher signal intensity from CO-Pt^{δ+} than CO-Pt⁰ in 50 Pt/Mo₂C indicate that CO-Pt^{δ+} sites dominated the electronic nature of Pt NPs, as depicted in Fig.2a (left), which is consistent with the fact that 50 Pt/Mo₂C possesses the highest Pt dispersion (57%) summarized in Table S1 and largest BE shift (0.70 eV) among all the Pt/Mo₂C

samples (Fig.S3). In contrast, dominating amount of Pt sites in 100 Pt/Mo₂C samples were not affected significantly by strain-ligand effect as the particles grow thicker, except for those along the peripheral interface and in the proximity with Mo₂C substrate (Fig. 2a, right). Consequently, CO-Pt⁰ signals were much stronger for 100 Pt/Mo₂C than for 50 Pt/Mo₂C, consistent with the much lower BE shift from Pt⁰ (0.22 eV) and significantly lower dispersion (41%).

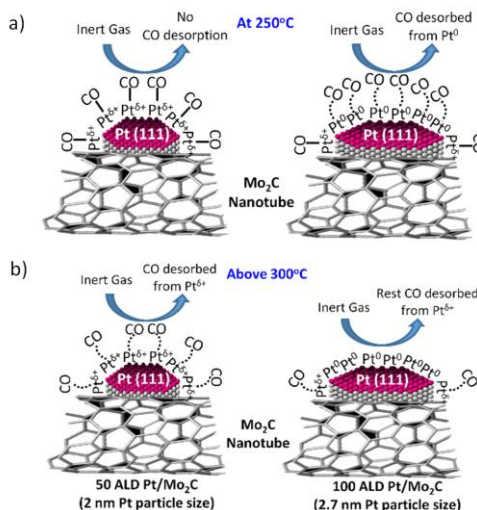


Figure 2. Schematic of CO desorption process at different temperatures for 50 (left) and 100 Pt/Mo₂C (right).

CO bond strength to Mo₂C sites provides another crucial indicator of surface properties. For 100 Pt/Mo₂C (Fig.1b), the intensities of CO-Mo₂C peaks decreased with longer helium (He) purging time at 150°C, indicating the removal of CO molecules from Mo₂C surface. This peak remained constant for over 20 minutes for both 50 and 100 Pt/Mo₂C till temperature increases to 200°C. However, these two samples responded differently with temperature increase. For 100 Pt/Mo₂C, CO molecules adsorbed on Mo₂C sites were removed substantially at 200°C, evidenced by the disappearance of CO-Mo₂C peaks (Fig. 1b). The intensity of CO-Mo₂C peaks in 50 Pt/Mo₂C sample only had a slight decrease when temperature increased to 200-250 °C and did not disappear until temperature increased to 300 °C. We postulate that the strong strain-ligand effect in the smaller and thinner 50 Pt/Mo₂C NPs may have affected the electronic structure Mo₂C sites, possibly forming Pt-Mo alloy.⁸

Similar trend with temperature was also observed for CO-Pt⁰ peaks. For 100 Pt/Mo₂C, intensity of the linear CO-Pt⁰ peaks remained constant at 200°C, but significantly decreased when temperature increased to 250°C and above, indicating desorption of CO molecules from Pt⁰ sites, as depicted in Fig.2a (right). It was also worth noting that these two peaks red-shifted to lower frequency with He purging time and temperature increase (dashed lines in Fig. 1b). This was attributed to dipole-dipole coupling change between CO and Pt atom as CO coverage decreased.^{19,26} The signal of CO-Pt⁰ for 50 Pt/Mo₂C is fairly weak, following a similar trend to 100 Pt/Mo₂C with He purging time. When temperature increased to 200°C, the signal further weakened to the noise level of DRIFTS. However, the dominating CO-Pt^{δ+} signal from 50 Pt/Mo₂C remained at 300°C and became sharper (Fig.1a), suggesting that CO desorption temperature from Pt^{δ+} sites is above 300°C (Fig.2b, left).

To correlate the CO-Pt⁰ and CO-Pt^{δ+} bond strength with catalytic activity, temporal analysis of products (TAP) reactor system²⁷ was used to carefully examine the effect of CO adsorption/desorption on CO oxidation step (CO→CO₂) by temperature programmed CO pulse response experiments. One advantage of transient experiments in vacuum is the higher time resolution that enables observation of subtle processes that could be missed in DRIFTS experiment. Following the removal of surface species during pretreatment process (see ESI for detail), the samples were exposed to CO pulses at room temperature first. High CO retention, shown in Fig.3, was detected for all samples with the greatest per pulse reaching 90% for the 50 Pt/Mo₂C sample. The CO molecules must be strongly bound to the surface because no gas phase products were detected. This enhanced CO interaction supports the strain-ligand effect hypothesis indicated by the XPS and DRIFTS results (Fig. S₃ and Fig.1). CO also interacts with the pristine Mo₂C and 100 Pt/Mo₂C sample at room temperature. However, for these materials CO₂ production was observed (Fig.3). Particularly for the bare Mo₂C material, a CO₂ fractional yield near 40% was detected. The carbon balance shows significant CO retention on the surface for all materials (Fig. 4a). The pronounced CO₂ production at room temperature from Mo₂C and 100 Pt/Mo₂C can be attributed to the forward Boudouard reaction (2CO → C + CO₂). Pulse response experiments using CO isotopes are needed to definitively rule out participation of the surface species. However, the participation of surface species is considered unlikely since sustained CO₂ production, as shown in Fig.S7, was observed for all samples as pulses continued with temperature being slowly increased at the same time.

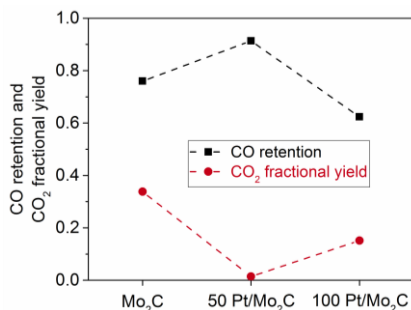


Figure 3. CO retention and CO₂ fractional yield when CO is pulsed at room temperature in vacuum.

When observing pulse response shape such as those in Fig.S7, the most obvious point of reference is the peak height. Although the CO₂ production rapidly drops for the Mo₂C sample (Fig.S7 a) in the initial pulses, indicating adsorption site poisoning through carbon accumulation, it remains sustained throughout the experiment. The carbon mass balance suggests a significant amount of the pulsed CO is not detected in the gas phase products and remains on the surface. A clearer interpretation of the CO and CO₂ pulse response data is presented in Fig.4, with the CO retention in each pulse and the CO₂ yield being indicated.

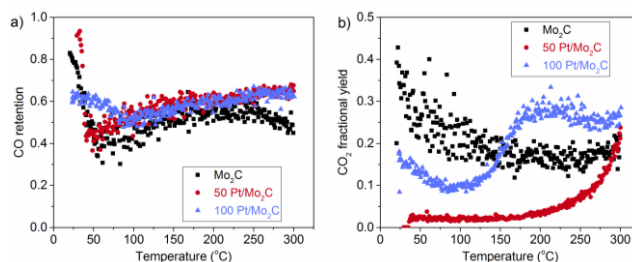


Figure 4. CO retention (a) and CO₂ fractional yield (b) for different samples.

All samples indicate an initial drop in CO retention when temperature increased from room temperature to 50°C, which could be attributed to site poisoning by C accumulation from the forward Boudouard reaction. As the temperature increases, however, there is a turning point (Fig.4a) where CO retention begins to increase (near 50°C for Mo₂C and 50 Pt/Mo₂C, near 100 °C for 100 Pt/Mo₂C). The CO₂ production for the Mo₂C sample continuously drops as the temperature is raised and plateaued around 150°C. The 50 Pt/Mo₂C sample maintains CO retention (Fig. 4a) but does not indicate CO₂ production until temperatures greater than 150°C are reached (Fig.4b). At 200°C the CO retention is still high while CO₂ production is low indicating that CO is strongly bound to the surface in corroboration with the CO-Pt^{δ+} peak for 50 Pt/Mo₂C in DRIFTS data (Fig. 1a). The fact that bare Mo₂C support and the 50 Pt/Mo₂C catalyst does not behave the same for CO₂ production suggests that the ALD deposited Pt NPs in 50 Pt/Mo₂C may have changed the electronic structure of the Mo₂C surface. The 100 Pt/Mo₂C sample indicates unique behavior for temperature dependent CO₂ production with a low temperature regime (100-275°C) transitioning to a higher temperature regime (>275°C) where CO₂ yield is pronounced (Fig.S7c and Fig.4b). This indicates the presence of distinct routes to CO₂ formation through different active sites, consistent with XPS (Fig.S₃), HRTEM (Fig.S₄) and DRIFTS results (Fig.2).

The particle size effect on catalytic activity was also investigated under WGS conditions using catalysts loading of 400 and 100 mg (Fig. 5 and Fig. S₉). Both 50 and 100 Pt/Mo₂C showed significantly enhanced CO conversion, compared to bare Mo₂C nanotubes. 50 Pt/Mo₂C generally required higher working temperature, which is very pronounced in the temperature range of 200-350°C and reflected by a slightly higher apparent activation energy (E_a) (55.8 kJ/mol) than that of 100 Pt/Mo₂C (53.6 kJ/mol) (Fig.S8). We attribute this to the fact that 50 Pt/Mo₂C has more substantial amount of Pt atoms affected by strain-ligand effect than 100 Pt/Mo₂C. The stronger bonding of CO-Pt^{δ+} required higher temperature to activate the Pt^{δ+} sites, which resulted in lower WGS rate in 50 Pt/Mo₂C than in 100 Pt/Mo₂C for low temperature range. However, when temperature increased above 300°C, 50 Pt/Mo₂C showed ~2.5 times higher WGS rate (0.82 mol CO/mol_{Pt}-s) than 100 Pt/Mo₂C (0.35 mol CO/mol_{Pt}-s). For the same reaction conditions, similar WGS rate trend was observed for lower catalyst loading (100 mg, Fig.S₉).

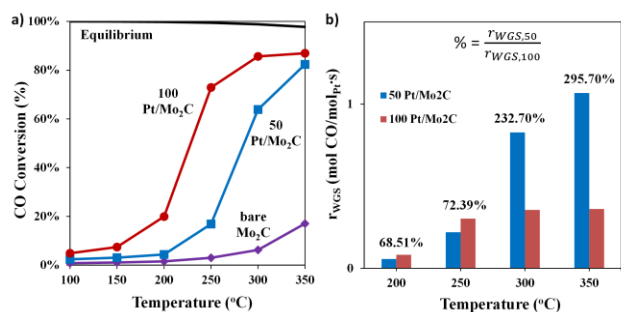


Figure 5. The CO conversion (a) and WGS rate (mol CO/mol_{Pt}·s) (b) of Pt/Mo₂C catalysts for WGS (12.5% CO-37.5% H₂O-50% N₂ feed condition at 15000 h⁻¹ GHSV).

To summarize, we demonstrated that Pt NPs deposited on phase-pure Mo₂C nanotube can be used as an experimental platform for elucidating active sites and electronic structure of both Pt and Mo₂C. The Pt particle size change in the range of < 3 nm not only resulted in core-level shift of the supported Pt, but may also have changed the electronic structure of nearby Mo₂C sites, suggested by different CO-Mo₂C bond strengths between 50 and 100 Pt/Mo₂C materials. The biggest BE shift from Pt^o for 50 Pt/Mo₂C materials was further corroborated by evident CO-Pt^{δ+} signal in DRIFTS and much higher CO₂ production temperature in TAP results. WGS rates suggest that there may be an optimal particle perimeter and thickness that balances working temperature and activity. Future study with X-ray absorption fine structure spectroscopy (XAFS) combined with DRIFTS²⁸ will facilitate further probing of the interface between Pt NP and TMC support with the reported Pt/Mo₂C catalyst platform.

ASSOCIATED CONTENT

Supporting Information

The detailed catalyst preparations, characterizations, TAP and WGS reaction measurements are included in the Electronic Supporting Information (ESI). This material is available free of charge via the Internet at <http://pubs.acs.org>.

AUTHOR INFORMATION

Corresponding Author

Department of Chemical Engineering, University of Wyoming, Laramie, WY, 82072. dliu@uwyo.edu.

ACKNOWLEDGMENT

We are grateful to Professors Joseph Holle, Maohong Fan and Dr. Erwin Sabio for their assistance with BET/chemisorption, DRIFTS and HRTEM/XPS experiments. We thank the Office of Research and Economic Development, School of Energy Research (SER) and NASA EPSCoR at the University of Wyoming for their generous financial support. We acknowledge of support of the U.S. Department of Energy, under DOE Idaho Operations Office Contract DE-AC07-05ID14517. Accordingly, the U.S. Government retains a nonexclusive, royalty-free license to publish or reproduce the published form of this contribution, or allow others to do so, for U.S. Government purposes.

REFERENCES

- Levy, R. B.; Boudart, M. *Science*. **1973**, *181* (4099), 547–549.
- Wan, C.; Regmi, Y. N.; Leonard, B. M. *Angew. Chemie Int. Ed.* **2014**, *53* (25), 6407–6410.
- Zhang, K.; Yang, W.; Ma, C.; Wang, Y.; Sun, C.; Chen, Y.; Duchesne, P.; Zhou, J.; Wang, J.; Hu, Y.; Banis, M. N.; Zhang, P.; Li, F.; Li, J.; Chen, L. *NPG Asia Mater.* **2015**, *7* (1), e153.
- Liu, Y.; Kelly, T. G.; Chen, J. G.; Mustain, W. E. *ACS Catal.* **2013**, *3* (6), 1184–1194.
- Hunt, S. T.; Milina, M.; Alba-rubio, A. C.; Hendon, C. H.; Dumesic, J. A.; Román-leshkov, Y. *Science* (80-). **2016**, *352* (6288), 974–978.
- Ma, Y.; Guan, G.; Hao, X.; Zuo, Z.; Huang, W.; Phanthong, P.; Li, X.; Kusakabe, K.; Abudula, A. *RSC Adv.* **2015**, *5* (20), 15002–15005.
- Patt, J.; Moon, D. J.; Phillips, C.; Thompson, L. *Catal. Letters* **2000**, *65*, 193–195.
- Sabnis, K. D.; Akatay, M. C.; Cui, Y.; Sollberger, F. G.; Stach, E. A.; Miller, J. T.; Delgass, W. N.; Ribeiro, F. H. *J. Catal.* **2015**, *330*, 442–451.
- Sabnis, K. D.; Cui, Y.; Akatay, M. C.; Shekhar, M.; Lee, W.-S.; Miller, J. T.; Delgass, W. N.; Ribeiro, F. H. *J. Catal.* **2015**, *331*, 162–171.
- Schaidle, J. a.; Lausche, A. C.; Thompson, L. T. *J. Catal.* **2010**, *272* (2), 235–245.
- Schweitzer, N. M.; Schaidle, J. a.; Ezekoye, O. K.; Pan, X.; Lincic, S.; Thompson, L. T. *J. Am. Chem. Soc.* **2011**, *133*, 2378–2381.
- Kitchin, J. R.; Nørskov, J. K.; Barteau, M. a.; Chen, J. G. *Phys. Rev. Lett.* **2004**, *93* (15), 4–7.
- Strasser, P.; Koh, S.; Anniyev, T.; Greeley, J.; More, K.; Yu, C.; Liu, Z.; Kaya, S.; Nordlund, D.; Ogasawara, H.; Toney, M. F.; Nilsson, A. *Nat. Chem.* **2010**, *2* (6), 454–460.
- Jia, Q.; Caldwell, K.; Strickland, K.; Ziegelbauer, J. M.; Liu, Z.; Yu, Z.; Ramaker, D. E.; Mukerjee, S. *ACS Catal.* **2015**, *5* (11), 176.
- Friebel, D.; Viswanathan, V.; Miller, D. J.; Anniyev, T.; Ogasawara, H.; Larsen, A. H.; Ogrady, C. P.; Nørskov, J. K.; Nilsson, A. *J. Am. Chem. Soc.* **2012**, *134* (23), 9664–9671.
- Xie, S.; Choi, S. Il; Lu, N.; Roling, L. T.; Herron, J. a.; Zhang, L.; Park, J.; Wang, J.; Kim, M. J.; Xie, Z.; Mavrikakis, M.; Xia, Y. *Nano Lett.* **2014**, *14* (6), 3570–3576.
- Peterson, E. J.; DeLaRiva, A. T.; Lin, S.; Johnson, R. S.; Guo, H.; Miller, J. T.; Hun Kwak, J.; Peden, C. H. F.; Kiefer, B.; Allard, L. F.; Ribeiro, F. H.; Datye, A. K. *Nature communications*. **2014**, p 4885.
- Setthapun, W.; Williams, W. D.; Kim, S. M.; Feng, H.; Elam, J. W.; Rabuffetti, F. a.; Poepelmeier, K. R.; Stair, P. C.; Stach, E. a.; Ribeiro, F. H.; Miller, J. T.; Marshall, C. L. *J. Phys. Chem. C* **2010**, *114* (21), 9758–9771.
- Ding, K.; Gulec, A.; Johnson, A. M.; Schweitzer, N. M.; Stucky, G. D.; Marks, L. D.; Stair, P. C. *Science* (80-). **2015**, *350* (6257), 1688–1690.
- Saha, S.; Martin, B.; Leonard, B.; Li, D. *J. Mater. Chem. A Mater. energy Sustain.* **2016**, *4*, 9253–9265.
- Hsu, I. J.; Hansgen, D. A.; Mccandless, B. E.; Willis, B. G.; Chen, J. G. *J. Phys. Chem. C* **2011**, *115* (9), 3709–3715.
- Mun, B.; Lee, C.; Stamenkovic, V.; Markovic, N.; Ross, P. *Phys. Rev. B* **2005**, *71* (11), 115420.
- Green, I. X.; Tang, W.; Neurock, M.; Yates Jr., J. T. *Science* (80-). **2011**, *333*, 736–740.
- Wang, J.; Kispersky, V. F.; Nicholas Delgass, W.; Ribeiro, F. H. *J. Catal.* **2012**, *289*, 171–178.
- Bazin, P.; Saur, O.; Lavalley, J. C.; Daturi, M.; Blanchard, G. *Phys. Chem. Chem. Phys.* **2005**, *7*, 187–194.
- Crossley, A.; King, D. A. *Surf. Coatings Technol.* **1977**, *68*, 528–538.
- Gleaves, J. T.; Yablonskii, G. S.; Phanawadee, P.; Schuurmanb, Y. *Appl. Catal. A Gen.* **1997**, *160*, 55–88.
- Brieger, C.; Melke, J.; Bosch, N. Van Der; Reinholz, U.; Riesemeier, H.; Guilherme, A.; Krishna, M.; Derr, I.; Schökel, A.; Roth, C. J. *Catal.* **2016**, *339*, 57–67.

For Table of Contents Only

